

## Projected reversal of oceanic stable carbon isotope ratio depth gradient with continued anthropogenic carbon emissions

Eun Young Kwon <sup>1,2</sup>, Axel Timmermann <sup>1,2</sup>, Brett J. Tipple <sup>3</sup> & Andreas Schmittner<sup>4</sup>

Paleoceanographic records suggest that the present-day vertical gradient in the stable carbon isotopic composition ( $\delta^{13}\text{C}$ ) of dissolved inorganic carbon in the ocean was reversed during the Paleocene-Eocene Thermal Maximum, an early period of relatively rapid release of carbon into the climate system. Here we present simulations from an observationally constrained ocean model under various greenhouse gas emissions scenarios. We project a decrease in the globally averaged  $\delta^{13}\text{C}$  of dissolved inorganic carbon in the surface ocean of between  $-1.8$  to  $-6.3$  ‰ by 2100. This reduction is driven by oceanic absorption of anthropogenic carbon dioxide, which is depleted in carbon-13. Our findings suggest an elimination or reversal of the natural vertical gradient in the  $\delta^{13}\text{C}$  of dissolved inorganic carbon by 2100 unless anthropogenic carbon emissions are reduced soon. We conclude that the Paleocene-Eocene Thermal Maximum is a geologic analogue of future global carbon cycle perturbations under continued rapid anthropogenic carbon emissions.

<sup>1</sup>Center for Climate Physics, Institute for Basic Science, Busan 46241, South Korea. <sup>2</sup>Pusan National University, Busan 46241, South Korea. <sup>3</sup>School of Biological Sciences, University of Utah, Salt Lake City, UT 84112, USA. <sup>4</sup>College of Earth, Ocean, and Atmospheric Sciences, Oregon State University, Corvallis, OR 97331-5503, USA. ✉email: [ekwon957@gmail.com](mailto:ekwon957@gmail.com)

Anthropogenic carbon (C) emissions have led to an accumulation of  $^{13}\text{C}$ -depleted carbon in the atmosphere and the upper ocean, diluting the isotopic composition of carbon dioxide ( $\text{CO}_2$ ) and dissolved inorganic carbon (DIC) (referred to as the  $^{13}\text{C}$  Suess effect)<sup>1,2</sup>. The oceanic absorption of anthropogenic  $\text{CO}_2$  has disturbed naturally formed vertical gradients of the  $\delta^{13}\text{C}$  of DIC ( $\delta^{13}\text{C}$ -DIC) where  $\delta^{13}\text{C}$  is defined as  $[(^{13}\text{C}/^{12}\text{C})_{\text{sample}}/(^{13}\text{C}/^{12}\text{C})_{\text{standard}} - 1]$  with the Vienna Pee Dee Belemnite standard. Surface seawater  $\delta^{13}\text{C}$ -DIC values are typically more positive relative to deep waters<sup>3,4</sup>, due primarily to the preferential downward transport of  $^{12}\text{C}$  relative to  $^{13}\text{C}$  by marine biota<sup>5</sup>. Vertical gradients of  $\delta^{13}\text{C}$ -DIC result from the interplay between the oceanic biological carbon pump, air-sea  $\text{CO}_2$  exchange rates, thermodynamic fractionations, and ocean circulation as well as rapid invasion of  $^{13}\text{C}$  depleted atmospheric  $\text{CO}_2$  (refs. 3,6–11). Because all of these controlling processes are sensitive to climate and environmental changes, the  $\delta^{13}\text{C}$ -DIC values recorded in marine carbonate fossils have been used to gain valuable insights into past changes of the global carbon cycle and ocean circulation<sup>4,8,10,12–15</sup>. However, the preindustrial  $\delta^{13}\text{C}$ -DIC distribution and its anthropogenic evolutions are uncertain<sup>1,16</sup>, due to the difficulty of accounting for the imprint of  $^{13}\text{C}$ -depleted emissions from fossil fuel burning and deforestation. These uncertainties in turn hinder projections of future oceanic  $\delta^{13}\text{C}$ -DIC, which can provide a long-term perspective of natural and human-induced changes in the global carbon cycle<sup>17</sup>.

The best known geologic analogue to the future perturbation of the global carbon cycle is the Paleocene-Eocene Thermal Maximum (PETM; ~56 million years ago)<sup>17</sup>, which was characterized by carbon isotope excursions of  $-(3\text{--}5)\%$  on the Earth's surface<sup>9,12,13</sup>. These anomalies were accompanied by rising temperatures and widespread ocean acidification, and have been attributed to a rapid carbon release of ~10,000 GtC to the climate system<sup>12,13,18</sup>. Foraminifera fossil  $\delta^{13}\text{C}$  records also suggest that the pre-PETM depth gradients might have been eliminated or even reversed during the PETM onset<sup>9,13</sup>. However, because the carbon emission rates for the PETM onset were estimated to be an order of magnitude slower than those during industrialization<sup>8,19,20</sup>, the PETM deep ocean might have had sufficient time to fully equilibrate to changing atmospheric  $\text{CO}_2$  without necessarily invoking a vertical gradient reversal<sup>8</sup>. Nonetheless, several studies<sup>8,11,21</sup> suggested that relatively rapid carbon emissions could have delayed deep ocean  $\delta^{13}\text{C}$ -DIC excursions compared to the surface, causing a temporal reversal of the vertical  $\delta^{13}\text{C}$ -DIC gradient. Such sensitivity indicates that the early geochemical evolution of the vertical  $\delta^{13}\text{C}$ -DIC gradient can provide an important constraint on the PETM onset duration, which has previously been suggested to be between 3 and 20 kyr<sup>8,19,20</sup>.

Here, we use an observationally constrained global oceanic carbon cycle model<sup>22,23</sup> and four representative concentration pathways (RCPs)<sup>24</sup> to estimate the temporally evolving oceanic  $\delta^{13}\text{C}$ -DIC from the preindustrial era to the 21st century (Methods). We find that the 21st century greenhouse gas emissions will induce elimination or even reversal of the natural vertical  $\delta^{13}\text{C}$ -DIC gradient by the end of the 21st century and elucidate the geochemical mechanisms underlying such radical changes in surface  $\delta^{13}\text{C}$ -DIC. Our 21st century projections combined with multi-millennial simulations for hypothetical futures now allow us to compare the  $\delta^{13}\text{C}$ -DIC excursions between the future and the PETM onset, which will benefit from a recent compilation<sup>25</sup> of the PETM foraminifera  $\delta^{13}\text{C}$  records.

## Results and discussion

**Modern ocean  $^{13}\text{C}$  Suess effect.** The oceanic  $\delta^{13}\text{C}$ -DIC changes from the preindustrial era to 2018 are assessed using a Monte

Carlo experiment (Methods), for which uncertainties in various model parameters (Supplementary Table 1) are allowed to propagate in our model into the  $\delta^{13}\text{C}$ -DIC simulations. According to the simulations, the globally averaged surface ocean  $\delta^{13}\text{C}$ -DIC decline relative to 1780 CE pre-industrial conditions amounts to  $-(1.1 \pm 0.2)\%$  as of 2018 (Fig. 1a), with 84% of the uncertainty arising from uncertainties in air-sea  $\text{CO}_2$  exchange rates and the atmospheric  $^{13}\text{C}$  Suess effect (Supplementary Fig. 1a; Supplementary Note 2). A dominance of air-sea  $\text{CO}_2$  exchange rates for the uncertainty is in line with a previous study<sup>26</sup> based on an Earth System Model which suggested that air-sea gas exchange rates alone explain 63% of the total variance of simulated oceanic  $^{13}\text{C}$  Suess effects over a time period of 1858–2008.

Our surface estimate is consistent with a previous model-based estimate of Schmittner et al.<sup>3</sup> who suggested a surface-averaged change of  $-0.67\%$  as of the 1990's and an observation-based estimate of  $-0.76 \pm 0.12\%$  as of 1992 by Sonnerup et al.<sup>27</sup>. On the other hand, our estimated  $^{13}\text{C}$  Suess effect is more negative than that of Eide et al.<sup>1</sup> who suggested a globally averaged  $^{13}\text{C}$ -depletion of only  $0.4\%$  at 200 m as of 1994 (Fig. 2c, e); yet would be consistent if the previous estimate is corrected for the uncertainty of  $0.15\text{--}0.24\%$  suggested by the same study<sup>1</sup> and a later independent study<sup>28</sup>. The rate of upper ocean  $\delta^{13}\text{C}$ -DIC decline has been accelerating since 1960, keeping up with the atmospheric  $\delta^{13}\text{C}$ - $\text{CO}_2$  change (Fig. 1a), which is also consistent with global ocean coral records<sup>29</sup>. Compared to the surface ocean  $^{13}\text{C}$  Suess effect, below a depth of 74 m of the water column (referred to as subsurface hereinafter) the averaged  $^{13}\text{C}$  Suess effect is considerably smaller, attaining an averaged value of only  $-0.2 \pm 0.1\%$  due mainly to slow exchange rates between surface and deep waters.

The most pronounced  $^{13}\text{C}$ -depletion in  $\delta^{13}\text{C}$ -DIC occurs in the subtropical surface waters, North Atlantic Deep Water, and global mode and intermediate waters (Fig. 2a). These surface regions are characterized by relatively higher sensitivities of surface DIC to increasing atmospheric  $\text{CO}_2$  (i.e., the lower Revelle factor; Fig. 3e). The higher sensitivities, together with longer exposure times to the atmosphere, lead to the highest accumulation rate of  $^{13}\text{C}$ -depleted anthropogenic  $\text{CO}_2$  (refs. 30,31). Relatively weaker depletion occurs in upwelling-dominated areas such as the subpolar surface waters, equatorial surface waters, and the Southern Ocean surface waters where mixing from below dilutes the anthropogenic imprints at the sea surface. As a result, the perturbation ratio (defined as the ratio of deviations from the respective preindustrial values) of surface  $\delta^{13}\text{C}$ -DIC to atmospheric  $\delta^{13}\text{C}$ - $\text{CO}_2$  exhibits a large latitudinal contrast depending on the oceanic uptake of  $\text{CO}_2$  and the air-sea equilibrium states relative to vertical mixing rates<sup>30,31</sup>. For example, as of 2000, the surface to atmospheric  $\delta^{13}\text{C}$  perturbation ratio ranges from 0.1 in the highly convective Southern Ocean to  $0.7 \pm 0.1$  in the relatively stable Northern Hemisphere subtropical gyres (Fig. 3b), in agreement with a previous study<sup>1</sup>.

The best estimate for the preindustrial  $\delta^{13}\text{C}$ -DIC distributions can be derived by combining our constrained oceanic  $^{13}\text{C}$  Suess effect with the contemporary  $\delta^{13}\text{C}$ -DIC observations<sup>4</sup> (Fig. 2b; Supplementary Fig. 2; Methods). This approach is chosen rather than using simulated preindustrial  $\delta^{13}\text{C}$ -DIC distributions due to the large sensitivity of the preindustrial  $\delta^{13}\text{C}$ -DIC estimates to a poorly constrained boundary condition of terrestrial carbon inputs<sup>23</sup> (Supplementary Fig. 1a) and the unexplored sensitivity to the biological carbon pump<sup>32</sup>. Compared to a recent study from Eide et al.<sup>33</sup>, our estimate suggests more  $^{13}\text{C}$ -enrichment in the Southern Hemisphere mode and intermediate waters with values attaining up to  $2.6 \pm 0.3\%$ , and more  $^{13}\text{C}$ -depletion at  $0.5 \pm 0.2\%$  in the Antarctic Bottom Water (Fig. 2b, d, f). The

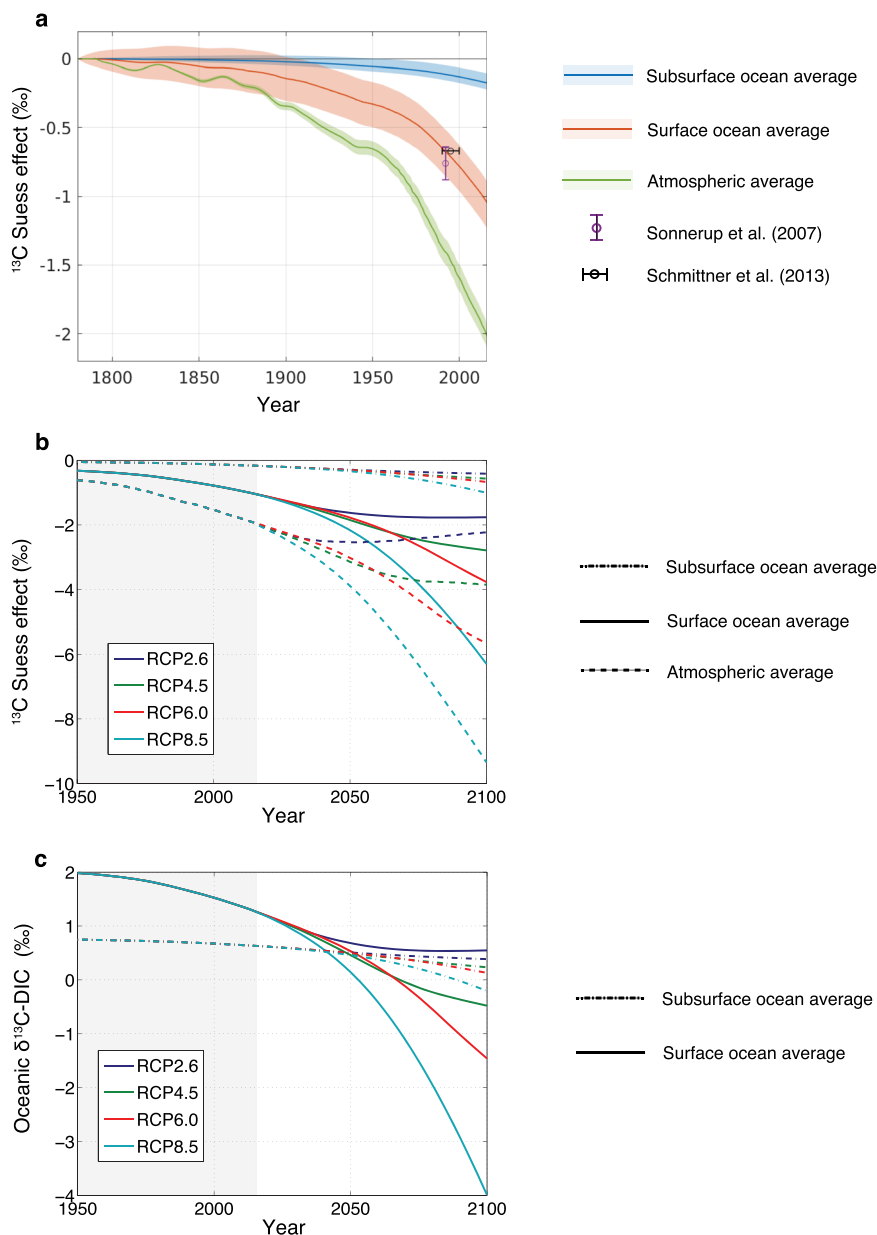


**Fig. 1 Globally averaged  $\delta^{13}\text{C}$  changes over time.** **a** The oceanic and atmospheric  $^{13}\text{C}$  Suess effect from 1780 to 2018, as represented by the  $\delta^{13}\text{C}$ -DIC and  $\delta^{13}\text{C}$ - $\text{CO}_2$  deviations from the preindustrial values, respectively. The subsurface (below a depth of 74 m) averaged  $^{13}\text{C}$  Suess effect is shown in blue line, the surface averaged  $^{13}\text{C}$  Suess effect is shown in red line, and the atmospheric Suess effect is shown in green line. Shading indicates a 95% confidence interval derived from the Monte Carlo experiment. **b** Estimated oceanic and atmospheric  $^{13}\text{C}$  Suess effects from 1950 to 2018 (gray-shaded background) are combined with the projected  $^{13}\text{C}$  Suess effects from 2019 to 2100. Four different colors indicate different  $\text{CO}_2$  concentration scenarios of RCP2.6 (purple), RCP4.5 (green), RCP6.0 (red), RCP8.5 (blue). Dashed lines show the atmospheric Suess effect, solid lines show the surface ocean averages, and dashed-dotted lines show the subsurface ocean averages. **c** Same as **b** except that the surface and subsurface ocean averaged  $\delta^{13}\text{C}$ -DIC values are shown.

relatively larger discrepancies in the Southern Hemisphere, compared to the Northern Hemisphere, may arise due to sparse observational coverage, which we argue makes the previous observation-based estimate more prone to uncertainty. Nevertheless, our results support a previous finding that surface water  $\delta^{13}\text{C}$ -DIC was more positive during preindustrial times than the present-day observations, revealing higher horizontal and vertical gradients associated with water mass distributions in the upper ocean<sup>33,34</sup>. Our preindustrial estimate of oceanic  $\delta^{13}\text{C}$ -DIC can serve as a reference state with which past estimates of oceanic  $\delta^{13}\text{C}$ -DIC (e.g.,  $\delta^{13}\text{C}$ -DIC during the Last Glacial Maximum, ~21,000 years ago) can be compared<sup>35</sup> (see data availability statement).

**Projected 21st century changes in  $\delta^{13}\text{C}$ -DIC.** We use four  $\text{CO}_2$  emission scenarios<sup>24</sup> and the linear relationship between the atmospheric  $\text{CO}_2$  and the  $\delta^{13}\text{C}$  of  $\text{CO}_2$  estimated based on the last decades of observations<sup>36</sup> (Supplementary Fig. 3) for the 21st century projections (Methods). Compared to the effects of the different  $\text{CO}_2$  emission scenarios (Fig. 1b), the effects of potential changes in air-sea  $\text{CO}_2$  exchange rates (another primary source of uncertainty identified for the estimated oceanic  $^{13}\text{C}$  Suess effect as of 2018) appear to be an order of magnitude smaller (Supplementary Figs. 4 and 5; Supplementary Note 3). Additional sources of uncertainty, including temporal changes in ocean circulation and the biological carbon pump, also appear to be minor for the 21st century changes in DIC and ocean pH, as shown by the close

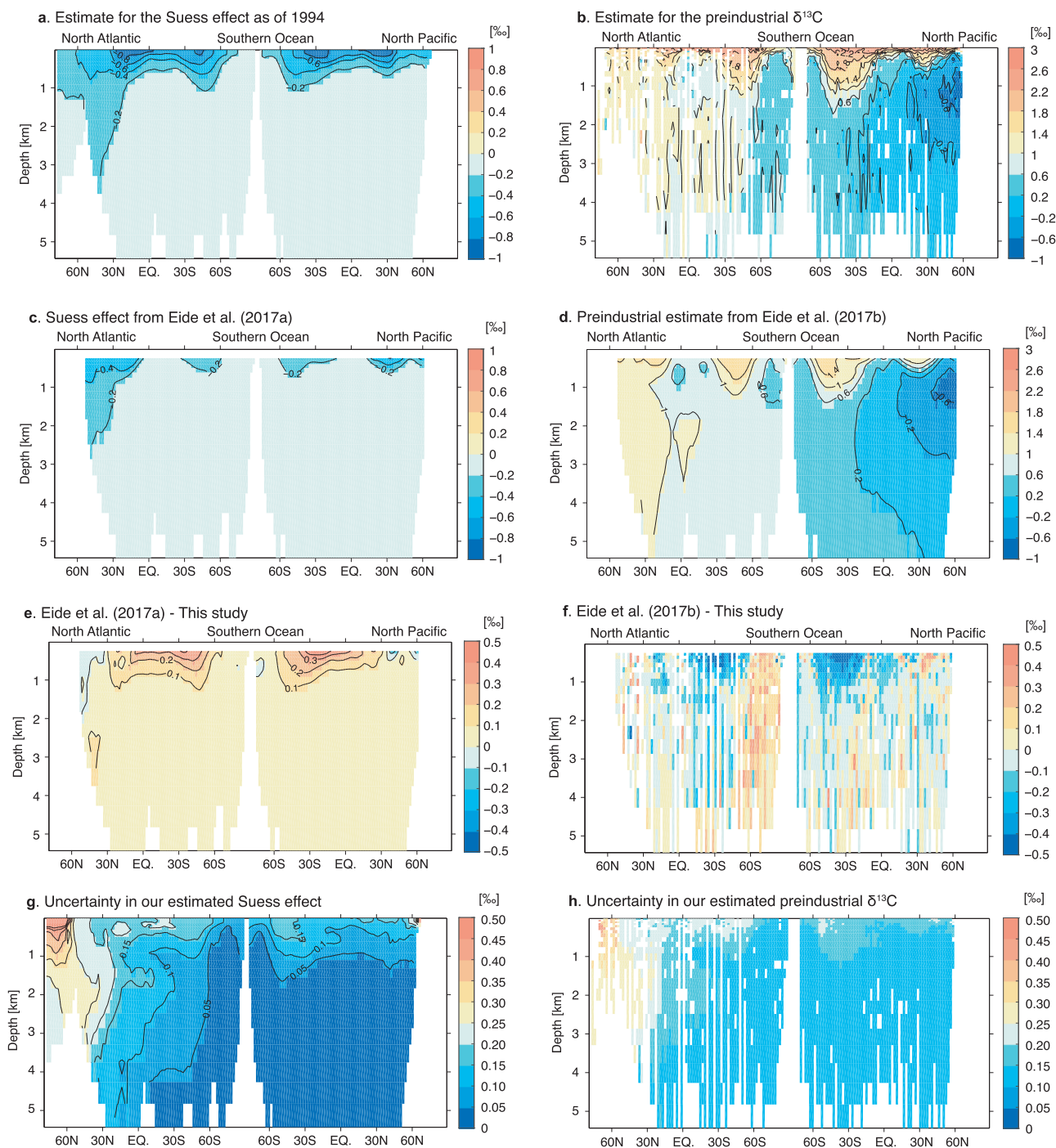


**Fig. 2** Zonally averaged vertical sections of  $\delta^{13}\text{C-DIC}$  from the North Atlantic to the Southern Ocean, and to the North Pacific. **a** Our estimate for the oceanic  $^{13}\text{C}$  Suess effect as of 1994. **b** Our estimate for the preindustrial  $\delta^{13}\text{C-DIC}$  obtained by correcting the global database<sup>4</sup> for the oceanic  $^{13}\text{C}$  Suess effect. **c** The oceanic  $^{13}\text{C}$  Suess effect estimated by Eide et al.<sup>1</sup> **d** The preindustrial  $\delta^{13}\text{C-DIC}$  estimated by Eide et al.<sup>33</sup> **e** Difference between Eide et al.<sup>1</sup> and our estimate. **f** Difference between Eide et al.<sup>33</sup> and our estimate. **g** The 95% confidence interval for our estimated  $^{13}\text{C}$  Suess effect. **h** The 95% confidence interval for our estimated preindustrial  $\delta^{13}\text{C-DIC}$ .

agreements between our estimates and those projected from multiple climate models<sup>37</sup> (Supplementary Fig. 6b). Likewise, the effects of ocean circulation and biological changes are likely small for the 21st century  $\delta^{13}\text{C-DIC}$  change<sup>26</sup>. The modulating effects of climate change on  $\delta^{13}\text{C-DIC}$  distributions may emerge on timescales that are longer than the timescales of the geochemical effects from rising atmospheric  $\text{CO}_2$  (refs. 11,38). Hence, we mainly focus on the effects of different  $\text{CO}_2$  emissions scenarios applied to the full model setup with time-invariant ocean

circulations and biogeochemical model parameters (Supplementary Table 1) for the 21st century  $\delta^{13}\text{C-DIC}$  projections.

All of the RCP scenarios suggest that oceanic  $\delta^{13}\text{C-DIC}$  becomes increasingly more  $^{13}\text{C}$ -depleted near the sea surface, as the ocean takes up more  $^{13}\text{C}$ -depleted atmospheric  $\text{CO}_2$  (Figs. 1b and 3a; Supplementary Fig. 7a). The globally averaged surface ocean  $^{13}\text{C}$  Suess effect is projected to range from  $-1.6\text{‰}$  for RCP2.6 to  $-2.2\text{‰}$  for RCP8.5 as of the year 2050. As time progresses, the surface ocean  $^{13}\text{C}$  Suess effect diverges to a range



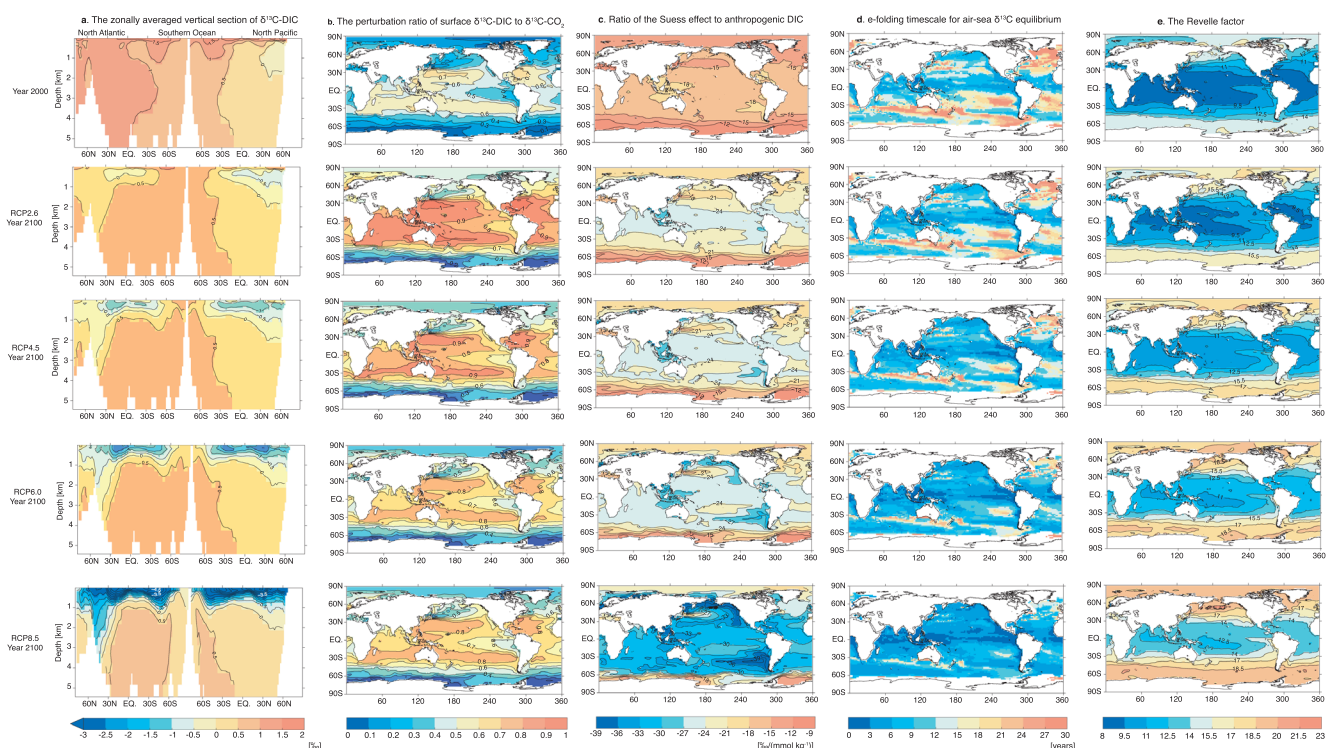


**Fig. 3 Simulated  $\delta^{13}\text{C}$ -DIC and ocean surface properties for different RCP scenarios.** The estimates as of 2000 are shown in the top row, the estimates as of 2100 are shown in the second (RCP2.6), third (RCP4.5), fourth (RCP6.0), and fifth (RCP8.5) rows. **a** The zonally averaged vertical sections of  $\delta^{13}\text{C}$ -DIC from the North Atlantic to the Southern Ocean, and to the North Pacific. **b** The ratios of surface  $\delta^{13}\text{C}$ -DIC perturbation to atmospheric  $\delta^{13}\text{C}$ - $\text{CO}_2$  perturbation where the perturbation is defined as a change since the preindustrial times. **c** The ratios of surface  $\delta^{13}\text{C}$ -DIC perturbation to DIC perturbation where the perturbation is defined as a change since the preindustrial times. **d** The e-folding timescale for the air-sea  $\delta^{13}\text{C}$  equilibrium, estimated as  $(\text{DIC}/\text{CO}_2^{\text{aq}}) \times (k_w/z_{\text{ml}})^{-1}$  where  $\text{CO}_2^{\text{aq}}$  is the aqueous  $\text{CO}_2$  concentrations at the sea surface,  $k_w$  is the piston velocity for air-sea  $\text{CO}_2$  exchange, and  $z_{\text{ml}}$  is the thickness of the mixed layer<sup>40</sup>. **e** The Revelle factor, defined as  $(\text{DIC}/\text{CO}_2) \times (\partial\text{CO}_2/\partial\text{DIC})$  where  $\text{CO}_2$  is oceanic  $\text{pCO}_2$ .

of  $-1.8$ – $6.3$ ‰ as of 2100 across the RCP scenarios. The perturbation ratios of surface  $\delta^{13}\text{C}$ -DIC to atmospheric  $\delta^{13}\text{C}$ - $\text{CO}_2$  also grow in time, reaching a maximum value greater than one at the center of the subtropical gyres under the RCP2.6 scenario that stabilizes atmospheric  $\text{CO}_2$  after 2040 (Fig. 3b). Accordingly, surface  $\delta^{13}\text{C}$ -DIC remains nearly constant between 2040 and 2100 (Fig. 1b). On the other hand, the perturbation ratio increases modestly in the RCP8.5 scenario (Fig. 3b) where the ocean surface does not have a sufficient time to equilibrate with the rapidly changing atmospheric  $\delta^{13}\text{C}$ - $\text{CO}_2$  (Fig. 1b; ref. 11).

The most pronounced and robust change towards the end of this century across the RCP scenarios is the appearance of the lowest  $\delta^{13}\text{C}$ -DIC values in the thermocline waters (shallower than a depth of 1000 m), which is evident in the global ocean low latitudes and the North Pacific high latitudes (Fig. 3a). The tropical and North Pacific high-latitude thermocline waters coincide with the regions of the highest accumulation rates of the  $^{13}\text{C}$ -depleted DIC remineralized from sinking organic particles, which contributed to the local minimum of the preindustrial  $\delta^{13}\text{C}$ -DIC (Fig. 2b). With the invasion of isotopically light anthropogenic carbon, the thermocline waters become further depleted in  $\delta^{13}\text{C}$ -DIC, emerging as new global  $\delta^{13}\text{C}$ -DIC minima. The thermocline  $\delta^{13}\text{C}$ -DIC minima gradually expand to the entire global ocean thermocline as time progresses.

Unlike the well-ventilated thermocline and relatively young North Atlantic Deep Water, the  $\delta^{13}\text{C}$ -DIC values in deep waters remain relatively unchanged with a subsurface averaged  $^{13}\text{C}$  Suess effect less than  $-1$ ‰ as of 2100 (Fig. 1b, c), becoming the waters of the most enriched  $\delta^{13}\text{C}$ -DIC. As a result, the naturally formed

vertical gradients of  $\delta^{13}\text{C}$ -DIC are eliminated or reversed towards the end of the 21st century. For example, the difference between the globally averaged surface and subsurface  $\delta^{13}\text{C}$ -DIC becomes  $0.2$ ‰ for RCP2.6,  $-0.7$ ‰ for RCP4.5,  $-1.6$ ‰ for RCP6.0, and  $-3.8$ ‰ for RCP8.5 as of 2100, compared to the preindustrial value of  $1.6 \pm 0.2$ ‰ (Figs. 1c and 3a). Such varying degrees of vertical gradient reversals indicate a large sensitivity of the gradient disruption to the rapidity of  $\text{CO}_2$  emissions, given the present-day ocean circulation rates. Furthermore, the regional magnitude of gradient reversal is larger in strongly stratified low latitude ocean than convective high latitudes, suggesting a sensitivity to ocean ventilation state as well (Fig. 3a). These reversed vertical gradients of  $\delta^{13}\text{C}$ -DIC are likely to persist at least over the next few centuries due to slow exchange rates between surface and deep waters and also to slow deep ocean circulation.

Projected global warming (e.g., ref. 39) is expected to further reduce surface  $\delta^{13}\text{C}$ -DIC through increasing air-sea  $\text{CO}_2$  exchange rates in high latitudes (mostly due to sea ice melting) and enhanced thermodynamic isotopic fractionations whose effects are most pronounced in low latitudes (Supplementary Fig. 5; Supplementary Note 3). These warming-driven surface  $\delta^{13}\text{C}$ -DIC reductions can additionally elevate the ratio of the ocean to atmosphere  $^{13}\text{C}$  Suess effect, and further, enhance the vertical  $\delta^{13}\text{C}$ -DIC gradient reversal as of 2100. When globally averaged, the warming effects are small with an additional surface  $\delta^{13}\text{C}$ -DIC decline of only  $-0.1$ ‰ compared to the geochemically driven  $^{13}\text{C}$  Suess effect of  $-3.7$ ‰ under the RCP6.0 scenario (Supplementary Fig. 4). Yet, regionally the effects can be as large as 50% in the Weddell Sea (Supplementary Fig. 5). A more comprehensive assessment of ocean stratification and circulation

change effects on  $\delta^{13}\text{C}$ -DIC projections remains a subject for future studies.

**Geochemical mechanisms for the ocean  $^{13}\text{C}$  Suess effect.** We elucidate the geochemical mechanisms by which the 21st century  $\text{CO}_2$  emissions can drive such radical changes in surface  $\delta^{13}\text{C}$ -DIC. The rapid evolution of the oceanic  $^{13}\text{C}$  Suess effect is somewhat surprising given that the ocean's ability to absorb anthropogenic  $\text{CO}_2$  in fact diminishes under higher DIC conditions (Fig. 3e). For example, under the RCP8.5 the surface-averaged  $^{13}\text{C}$  Suess effect increases eight times from  $-0.8\text{‰}$  in 2000 to  $6.2\text{‰}$  in 2100 (Fig. 1b), whereas the surface-averaged anthropogenic DIC increases four times from  $40$  to  $201 \mu\text{mol kg}^{-1}$  over the same time period (Supplementary Fig. 8b). The perturbation ratios of the surface  $\delta^{13}\text{C}$ -DIC to DIC also increase regionally by up to a factor of two from  $-15\text{‰}$  per a  $1 \text{ mmol kg}^{-1}$  increase in 2000 to  $-30\text{‰}$  per a  $1 \text{ mmol kg}^{-1}$  increase in 2100 under the RCP8.5 (Fig. 3c). Similarly, the perturbation ratio of surface  $\delta^{13}\text{C}$ -DIC to pH increases as the surface ocean becomes more acidic (Supplementary Fig. 6a, c). The progressively amplified response of surface  $\delta^{13}\text{C}$ -DIC, relative to surface DIC or pH, manifests as sharper vertical gradients for the  $^{13}\text{C}$  Suess effect than anthropogenic DIC<sup>30</sup>. As a result, the vertical gradient of oceanic  $\delta^{13}\text{C}$ -DIC undergoes more radical changes by the end of the 21st century, while the difference between the surface- and subsurface-averaged DIC decreases moderately by 20–70% (Supplementary Fig. 8c).

The amplified response of  $\delta^{13}\text{C}$ -DIC, compared to  $^{12}\text{C}$ , results from changes in seawater chemistry under higher  $\text{CO}_2$  conditions. Elevated surface DIC brings surface  $\delta^{13}\text{C}$ -DIC closer to an equilibrium with atmospheric  $\delta^{13}\text{C}$ - $\text{CO}_2$  through the dependency of the air-sea exchange rates of  $^{13}\text{C}/^{12}\text{C}$  on DIC speciation<sup>40</sup>. The globally averaged e-folding timescale, with which surface  $\delta^{13}\text{C}$ -DIC would approach a value in equilibrium with the atmosphere in the absence of other sources and sinks, decreases from 14 years as of the year 2000 to 6–12 years as of the year 2100 (with the smallest reduction in RCP2.6 and the largest in RCP8.5) (Fig. 3d). The enhanced air-sea  $\delta^{13}\text{C}$  equilibration rates can, in turn, facilitate the surface ocean Suess effect through either allowing for the surface ocean to catch up with atmospheric  $\delta^{13}\text{C}$ - $\text{CO}_2$  changes or alleviating the  $\delta^{13}\text{C}$ -DIC disequilibrium effects on a natural component of  $\delta^{13}\text{C}$ -DIC. These mechanisms are demonstrated in the following two idealized numerical experiments.

In the idealized fixed atmospheric  $\text{CO}_2$  experiment, we fix the atmospheric  $\text{CO}_2$  at a preindustrial value of 280 ppm while depleting the atmospheric  $\delta^{13}\text{C}$ - $\text{CO}_2$  over time as in the full model setup. In this experiment, the oceanic DIC and air-sea  $\delta^{13}\text{C}$  equilibration rates remain fixed at their preindustrial values in all RCP scenarios. This experiment yields the surface-averaged  $^{13}\text{C}$  Suess effects that account for 60–80% of the  $^{13}\text{C}$  Suess effects from the full model setup for the year of 2100 (Fig. 4). The remaining 20–40% (with the lowest value in RCP2.6 and the highest in RCP8.5) can be attributed mainly to the effect of enhanced air-sea equilibrium rates on  $\delta^{13}\text{C}$ -DIC, which facilitates the upper ocean depletion of  $\delta^{13}\text{C}$ -DIC.

To further explore the effect of enhanced air-sea equilibration rates on the natural component of  $\delta^{13}\text{C}$ -DIC, we perform an additional idealized experiment by fixing the atmospheric  $\delta^{13}\text{C}$ - $\text{CO}_2$  (or the ratio of  $^{13}\text{C}/^{12}\text{C}$ ) at a preindustrial value of  $-6.5\text{‰}$  while atmospheric  $\text{CO}_2$  increases as in the full model setup. The oceanic  $^{13}\text{C}$  Suess effect from this fixed atmospheric  $\delta^{13}\text{C}$ - $\text{CO}_2$  setup is nearly negligible when globally averaged, and also small regionally with the estimated  $^{13}\text{C}$  Suess effects that are an order of magnitude smaller than the Suess effects from the full

model setup (Supplementary Fig. 7b). Yet, such modulations of the natural component of  $\delta^{13}\text{C}$ -DIC are interesting because  $^{13}\text{C}$ -depletion in low latitudes are accompanied by opposing  $^{13}\text{C}$ -enrichments in high latitudes (north of  $40^\circ\text{N}$  or south of  $40^\circ\text{S}$ ) and deep waters, suppressing the subsurface  $^{13}\text{C}$  Suess effect through deep water formation in high latitudes. This geochemically driven enrichment effect, which depends on the magnitude of  $\text{CO}_2$  increases (Supplementary Fig. 7b), can retard deep ocean  $\delta^{13}\text{C}$ -DIC responses to atmospheric  $\delta^{13}\text{C}$ - $\text{CO}_2$  depletion on millennial timescales (Fig. 5c; See below).

**Comparison with PETM depth gradient reversal.** The magnitudes of our projected surface  $\delta^{13}\text{C}$ -DIC excursion as of 2100 for the intermediate to high emission scenarios are comparable with the PETM carbon isotope excursion of  $-(3\text{--}5)\text{‰}$  (Fig. 1b). The projected elimination or reversal of the vertical  $\delta^{13}\text{C}$ -DIC gradients (Fig. 1c) are also qualitatively similar to the reported changes in the benthic-planktic  $\delta^{13}\text{C}$ -DIC contrasts during the PETM onset<sup>9,13</sup>. Beyond the 21st century, future evolutions of oceanic  $\delta^{13}\text{C}$ -DIC are highly uncertain due to uncertainty in future atmospheric  $\text{CO}_2$  changes and potential feedbacks from the ocean. Yet, our multi-millennial simulations for hypothetical futures, assuming constant atmospheric  $\text{CO}_2$  after a year of 2500 and also considering geochemical effects only, reveal that the magnitude and duration of the gradient reversals are sensitive to the atmospheric  $\delta^{13}\text{C}$ - $\text{CO}_2$  excursions and the local ventilation states of the ocean. The surface ocean  $\delta^{13}\text{C}$ -DIC might drop by up to  $\sim 2\text{‰}$  under RCP2.6,  $\sim 4\text{‰}$  under RCP4.5, and up to  $\sim 6\text{‰}$  under RCP6.0, which outpace deep ocean  $\delta^{13}\text{C}$ -DIC decreases of similar magnitudes (Fig. 6a). The duration over which the gradient reversal persists ranges from none under RCP2.6 to a few millennia in poorly ventilated deep North Pacific under RCP6.0 and RCP8.5 (Fig. 6a; Supplementary Fig. 9).

Analogous to the future projections, Fig. 6b, c shows that reversal or at least elimination of the oceanic vertical  $\delta^{13}\text{C}$ -DIC gradients are evident in all pairs of planktic and benthic foraminifera species from two open-ocean sites (ODP Sites 690 and 1209) where high-resolution PETM records are currently available<sup>25</sup>. A precise comparison of the  $\delta^{13}\text{C}$ -DIC excursions between the future and the PETM onset is hampered due to the difficulty in reconstructing high temporal resolution PETM  $\delta^{13}\text{C}$  records (e.g., refs. 25,41) and large uncertainties in age models (e.g., refs. 42,43). In particular, benthic foraminiferal extinction and  $\text{CaCO}_3$  dissolution that might have led to data gaps during the PETM onset challenge a precise determination of the magnitude and duration of the vertical gradient reversal (e.g., ref. 18). Century-scale reversal or elimination events that are likely to occur under some RCP scenarios would not be detected in a typical pelagic deep ocean sediment core. Nevertheless, it is worth exploring whether the observed  $\delta^{13}\text{C}$ -DIC gradient reversal is consistent with previously suggested carbon emission rates during the PETM onset. For this, we apply the following two emission estimates to our model: a relatively rapid increase in atmospheric  $\text{CO}_2$  over 5 kyr<sup>19</sup> and a slow increase over 20 kyr<sup>8</sup>. In doing so, it is important to consider different ocean ventilation states, because the duration and magnitude of the vertical  $\delta^{13}\text{C}$ -DIC gradient reversals are also sensitive to ocean stratification and ventilation rates<sup>11,21</sup>.

Our sensitivity experiments (Methods) suggest that the surface to deep (average over 2–3 km depth) gradient reversal only occurs when an ocean model with poorly ventilated deep waters (an average ventilation age three times longer than the present-day ocean) is forced with rapidly increasing atmospheric  $\text{CO}_2$  over 5 kyr (Fig. 5a, b; Supplementary Fig. 9). While the surface and well-ventilated deep waters keep up with the atmospheric

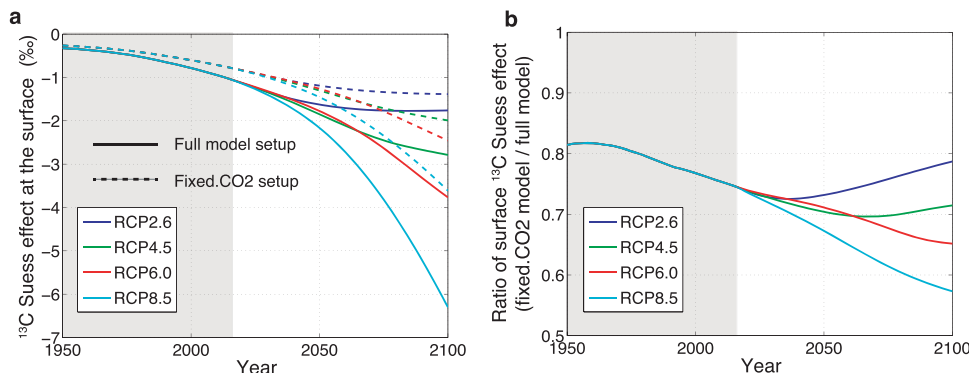


**Fig. 4 Comparison of surface ocean  $^{13}\text{C}$  Suess effect between the fixed atmospheric  $\text{CO}_2$  setup and the full model setup.** The fixed atmospheric  $\text{CO}_2$  setup is the same as the full model setup except that atmospheric  $p\text{CO}_2$  is fixed at 280 ppm while the  $\delta^{13}\text{C}$  of atmospheric  $\text{CO}_2$  changes over time as in the full model setup. Simulations prior to the year of 2019 are shown on the gray-shaded background. **a** Surface-averaged oceanic  $^{13}\text{C}$  Suess effects are shown in solid lines for the full model setup and in dashed lines for the fixed atmospheric  $\text{CO}_2$  setup. Four different colors indicate different  $\text{CO}_2$  emission scenarios of RCP2.6 (purple), RCP4.5 (green), RCP6.0 (red), RCP8.5 (blue). **b** The surface averaged  $^{13}\text{C}$  Suess effects from the fixed atmospheric  $\text{CO}_2$  experiment are divided by the respective Suess effects from the full model setup.

$\delta^{13}\text{C}$ - $\text{CO}_2$  change, the  $\delta^{13}\text{C}$ -DIC responses of stagnant deep waters (i.e., the North Pacific in the present-day configuration) are substantially delayed, temporally reversing the  $\delta^{13}\text{C}$ -DIC depth gradients. The simulated magnitude and duration of the vertical gradient reversal are comparable with those from a PETM record (the lower panel of Fig. 6b), and exhibit strong sensitivity to the atmospheric  $\delta^{13}\text{C}$ - $\text{CO}_2$  excursions (Fig. 5b). On the other hand, no discernible gradient reversal is simulated in the present-day ocean circulation state with deep ocean ventilation ages <1400 years (Fig. 5a), except for some localized reversals (Supplementary Fig. 10).

Under scenarios of slowly increasing atmospheric  $\text{CO}_2$  over 20 kyr (ref. 8), no reversals of the vertical  $\delta^{13}\text{C}$ -DIC gradient are apparent even in poorly ventilated regions (Fig. 5c). Slow increases in atmospheric  $\text{CO}_2$  (even slower than the vertical ocean mixing timescales) give the deep ocean sufficient time to fully equilibrate to changing atmospheric  $\text{CO}_2$ . Interestingly, the deep ocean  $\delta^{13}\text{C}$ -DIC exhibits distinct responses to the same atmospheric  $\delta^{13}\text{C}$ - $\text{CO}_2$  excursion of  $-4\text{‰}$  between the  $\times 5$  scenario where atmospheric  $\text{CO}_2$  increases approximately fivefold and the  $\times 2$  scenario where atmospheric  $\text{CO}_2$  increases approximately twofold (Fig. 5c). The  $^{13}\text{C}$  enrichment effect in high-latitude surface from enhanced air-sea  $\delta^{13}\text{C}$  equilibrium tends to offset the depleting effect from the invasion of  $^{13}\text{C}$ -depleted  $\text{CO}_2$ . This offset is greater in the  $\times 5$  scenario than in the  $\times 2$  scenario, such that during the perturbation period the vertical  $\delta^{13}\text{C}$ -DIC gradients become eliminated in relatively well-ventilated regions (i.e., the North Atlantic in the present-day configuration) under the  $\times 5$  scenario (Fig. 5c).

The evidence of a pronounced vertical gradient reversal at the ODP Site 690 (Fig. 6b), therefore, supports a rapid carbon emission rate towards a 5 kyr perturbation period and also suggests more stagnant deep waters during the PETM onset with slower ventilation rates than the present-day ventilation rates. Our inference is in agreement with previous studies<sup>44,45</sup> suggesting an overall decline in deep ocean ventilation rates during the PETM onset, possibly linked with the reorganization of deep ocean circulation patterns<sup>10,46,47</sup>. There remain important aspects of the observed PETM  $\delta^{13}\text{C}$ -DIC excursion that are not captured by our simulation, including much delayed and reduced declines in benthic  $\delta^{13}\text{C}$ , slight  $^{13}\text{C}$ -enrichments in benthic  $\delta^{13}\text{C}$  prior to declines, and different magnitudes of benthic  $\delta^{13}\text{C}$  declines between the two ODP sites (Fig. 6b, c). These disparities imply that concomitant transient changes in ocean circulation, marine biology, land-derived carbon inputs,

and marine sedimentary dissolutions of  $\text{CaCO}_3$  might have been as important as the geochemical effects for the early PETM  $\delta^{13}\text{C}$  excursion (e.g., refs. 10,11,21,44). In fact, Kirtland Turner and Ridgwell<sup>11</sup> showed that the  $\text{CO}_2$ -climate feedbacks during the PETM onset can delay the time that it takes for the surface  $\delta^{13}\text{C}$ -DIC minimum to propagate to the deep ocean  $\delta^{13}\text{C}$ -DIC minimum by up to 40%.

Despite the analogy between the future and the PETM onset in terms of large oceanic  $\delta^{13}\text{C}$ -DIC excursions and the existence of vertical gradient reversal, the rate at which the 21st century anthropogenic carbon isotope excursion occurs is at least one order of magnitude faster than PETM excursion rates. The 21st century  $\delta^{13}\text{C}$ -DIC gradient reversal rates (taking only  $\sim 3$  centuries from the preindustrial era to the maximum surface  $\delta^{13}\text{C}$ -DIC excursion) (Fig. 6a) appear to be much faster than those of the PETM (taking at least 3 kyr from the pre-PETM to the maximum surface  $\delta^{13}\text{C}$ -DIC excursion) (Fig. 6b, c). Given the fact that the PETM is the best known geological period when the most rapid carbon emissions have occurred over the Cenozoic (e.g., refs. 20,48), our comparison suggests that the time rates of 21st century  $\delta^{13}\text{C}$ -DIC excursion and associated gradient reversal may be unprecedented over the Cenozoic.

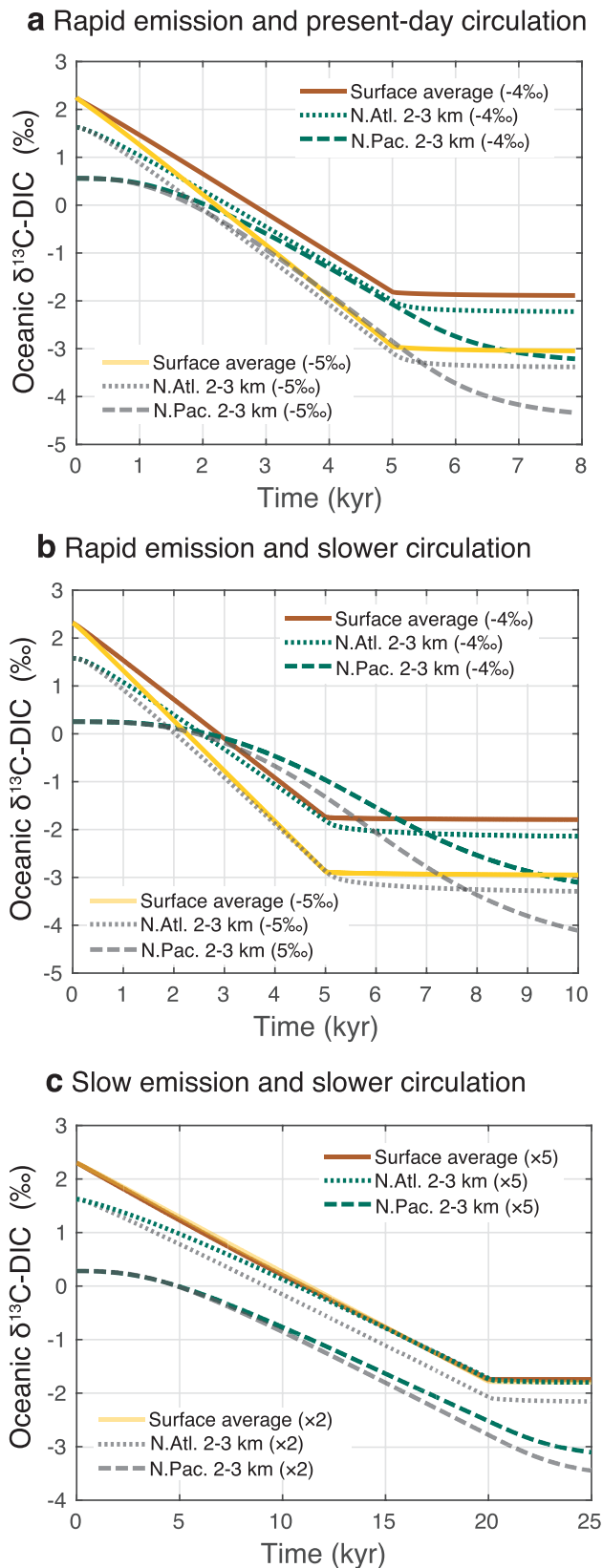
## Methods

**The ocean carbon cycle model.** We use an offline global ocean carbon cycle model<sup>23</sup> where a simple ocean biogeochemistry module is embedded in an observationally constrained ocean circulation inverse model (OCIM)<sup>22</sup>. The model has a horizontal resolution of  $2^\circ \times 2^\circ$  and a total of 24 vertical layers where the layer thickness increases from 36 m near the top to 633 m near the bottom. The circulation model uses a simplified version of the primitive equations using hydrostatic, rigid lid, and Boussinesq approximation, and produces ocean transport estimates that are optimally consistent with various observations of temperature, salinity, CFC-11, radiocarbon<sup>22</sup>. Large-scale ocean circulation and ventilation features are shown to be consistent with independent observation-based estimates<sup>49</sup> (See also Supplementary Fig. 10 for the simulated deep ocean ventilation age).

The ocean biogeochemical processes are formulated following the OCMIP2 protocol<sup>50</sup> where ocean productivity is simulated by restoring model surface  $\text{PO}_4$  towards the observed  $\text{PO}_4$ . Simple parameterizations for the production and remineralization of organic and inorganic carbon are employed. The carbon isotope model uses two prognostic variables of  $\text{DI}^{13}\text{C}$  and  $\text{DI}^{12}\text{C}$  (the latter approximated as DIC), and the isotopic signature of DIC is estimated as  $\delta^{13}\text{C}\text{-DIC} = [(\text{DI}^{13}\text{C}/\text{DI}^{12}\text{C})_{\text{sample}} / (\text{DI}^{13}\text{C}/\text{DI}^{12}\text{C})_{\text{standard}} - 1]$  with the Vienna Pee Dee Belemnite standard. The model employs a temperature-dependent thermodynamic equilibrium fractionation from Zhang et al. 7 and a  $\text{CO}_2$ -dependent photosynthetic fractionation following three different empirical formulations (Supplementary Table 1). The model includes riverine carbon inputs and a simple parameterization for the sedimentary burial of inorganic carbon.

Preindustrial steady-state solutions are obtained using a time-efficient Newton's method<sup>51</sup> whereas industrial changes are simulated by taking time steps with an





atmospheric CO<sub>2</sub> forcing taken from observation-based estimates<sup>36,52</sup> for a time period of 1780–2018 and RCP scenarios<sup>24</sup> for a time period of 2019–2100. Our model is based on an annual mean climatology that is invariant over time except for the atmospheric CO<sub>2</sub> and δ<sup>13</sup>C-CO<sub>2</sub> forcing that change over industrial times. The model was previously shown to simulate the oceanic uptake and storage of anthropogenic carbon<sup>22</sup>, as well as the oceanic <sup>13</sup>C Suess effect<sup>23</sup> (Fig. 1a), consistent with previous independent estimates. We refer readers to Kwon et al.<sup>23</sup>

**Fig. 5 Simulated responses of oceanic δ<sup>13</sup>C-DIC to the different atmospheric CO<sub>2</sub> and δ<sup>13</sup>C-CO<sub>2</sub> forcing previously suggested for the early PETM.** Surface δ<sup>13</sup>C-DIC values averaged over the global ocean are shown in solid lines. The deep (2–3 km depths) ocean δ<sup>13</sup>C-DIC values averaged over the North Atlantic (N.Atl., north of 20°N) and North Pacific (N.Pac., north of 20°N) are shown in dotted and dashed lines, respectively. **a** Results from the rapid PETM carbon emission setup where atmospheric CO<sub>2</sub> linearly increases twofold over 5 kyr according to Penman et al.<sup>69</sup> with maximum atmospheric δ<sup>13</sup>C-CO<sub>2</sub> excursions of −4‰ (red and green) and −5‰ (yellow and gray). We use the present-day ocean circulation state. **b** Same as **a** except that we use an ocean circulation state with slower ventilation rates (an average three fold increase in ventilation ages). **c** Results from the slow PETM carbon emission setup where atmospheric δ<sup>13</sup>C-CO<sub>2</sub> decreases by 4‰ over 20 kyr according to Cui et al.<sup>8</sup> with two different magnitudes of atmospheric CO<sub>2</sub> increases as suggested by Cui et al.<sup>8</sup>. Atmospheric CO<sub>2</sub> is assumed to linearly increase five fold over 20 kyr in red and green lines (×5) and twofold in yellow and gray lines (×2). We use the ocean circulation state of slower ventilation rates, as used in (**b**).

and Supplementary Note 1 for details of the carbon isotope model formulations. Although our primary focus is the geochemical effects from changing atmospheric CO<sub>2</sub>, our offline model framework allows us to perform an experiment where some of the biogeochemistry model inputs are taken from results of an Earth System Model (Supplementary Note 3).

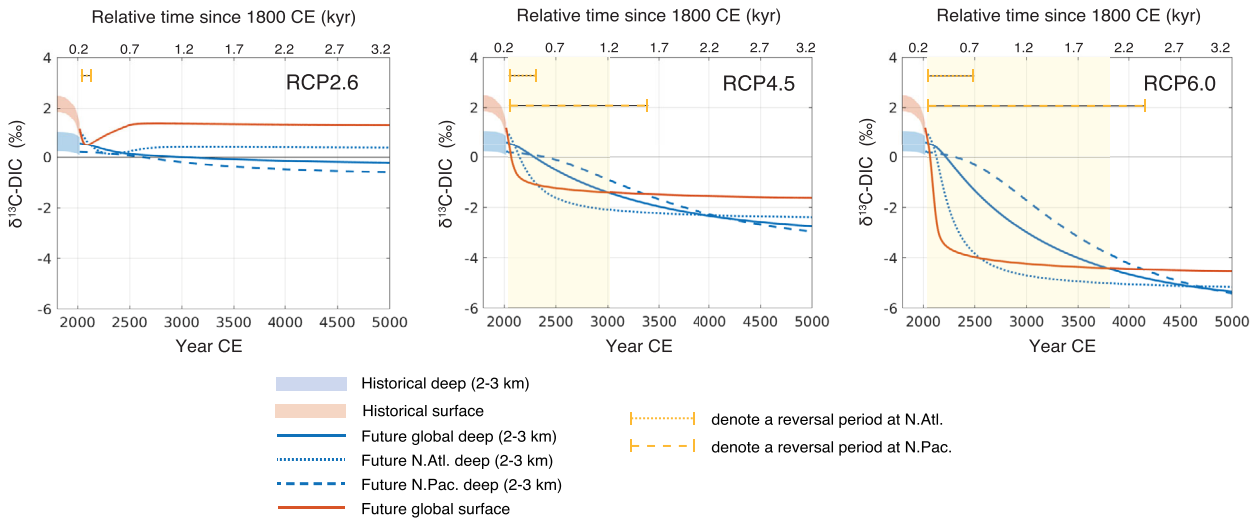
**A Monte Carlo experiment for historical simulations.** In order to explore a wide range of potential sources of uncertainty in simulating the oceanic δ<sup>13</sup>C-DIC until 2018, we perform a Monte Carlo experiment of 1400 ensemble members where the model parameter values and setups are randomly drawn from plausible ranges that are assumed to be uniformly distributed (Supplementary Table 1). Potential sources of uncertainty considered in this study include (A) preindustrial δ<sup>13</sup>C values for atmospheric CO<sub>2</sub> of −(6.3–6.5)‰<sup>53</sup>, which combined with observed values over 1980–2018 determine the atmospheric <sup>13</sup>C Suess effect over industrial times, (B) temperature-dependent thermodynamic equilibrium fractionation factors for air-sea CO<sub>2</sub> exchange<sup>7</sup> and time-varying sea surface temperatures over industrial times<sup>54–56</sup>, (C) the globally uniform δ<sup>13</sup>C values of riverine carbon inputs of −27 ± 2‰ for dissolved organic carbon, −30 ± 2‰ for particulate organic carbon, and −15 ± 2‰ for DIC<sup>57</sup>, (D) the magnitude of non-riverine terrestrial carbon inputs with a δ<sup>13</sup>C value of −26‰<sup>58</sup>, including uncertainties in groundwater driven fluxes<sup>59</sup> and the carbon export from coastal vegetation<sup>60</sup>, that are assumed to be uniformly distributed along the coastal margins except around the Antarctica, (E) the air-sea CO<sub>2</sub> exchange rates formulated following Wanninkhof<sup>61</sup> and Najjar et al.<sup>50</sup>, which are linearly scaled such that the globally averaged transfer rate ranges between 13 and 17 cm h<sup>−1</sup> (refs. 62,63), (F) CO<sub>2</sub> dependent fractionation factors for the photosynthetic uptake of carbon, taken from the three different empirical formulations<sup>5,64,65</sup>, (G) present-day ocean circulation states including different mixing parameterizations<sup>22</sup>, and (H) the amount of inorganic carbon buried in marine sediments<sup>66</sup> (See Supplementary Note 1 for the model parameters). Using the Monte Carlo experiment, a median value with a 95% confidence interval (two times one standard deviation) is reported for the estimated <sup>13</sup>C Suess effect and DIC change. We also perform regression analyses using the model input parameter values and the corresponding model estimates to explore the relative contributions of the different sources to uncertainty.

**Estimation of preindustrial δ<sup>13</sup>C-DIC.** We estimate a preindustrial δ<sup>13</sup>C-DIC distribution by combining the global compilation<sup>4</sup> of observed δ<sup>13</sup>C-DIC over 1972–2016 with our estimated oceanic <sup>13</sup>C Suess effect. We first map the observed δ<sup>13</sup>C-DIC onto our 2° × 2° model grid cells by averaging all data points falling within each grid cell at each year. To obtain a climatological mean distribution, we average the gridded data over time such that each grid cell has an averaged year of data collection and an averaged δ<sup>13</sup>C-DIC value (Supplementary Fig. 2a). Then, the mapped δ<sup>13</sup>C-DIC is corrected for the <sup>13</sup>C Suess effect with our estimate that is taken from the averaged year of data collection for each grid cell (Supplementary Fig. 2c). The uncertainty of the resulting preindustrial δ<sup>13</sup>C-DIC estimate (Fig. 2h) includes two standard mapping errors for the present-day δ<sup>13</sup>C-DIC observations, measurement uncertainties of ±0.1‰, and the uncertainty in our estimated <sup>13</sup>C Suess effect (Fig. 2g). This approach gives a preindustrial state of δ<sup>13</sup>C-DIC (Fig. 2b; Supplementary Fig. 2b) that is similar to our simulated preindustrial δ<sup>13</sup>C-DIC with reduced uncertainty.

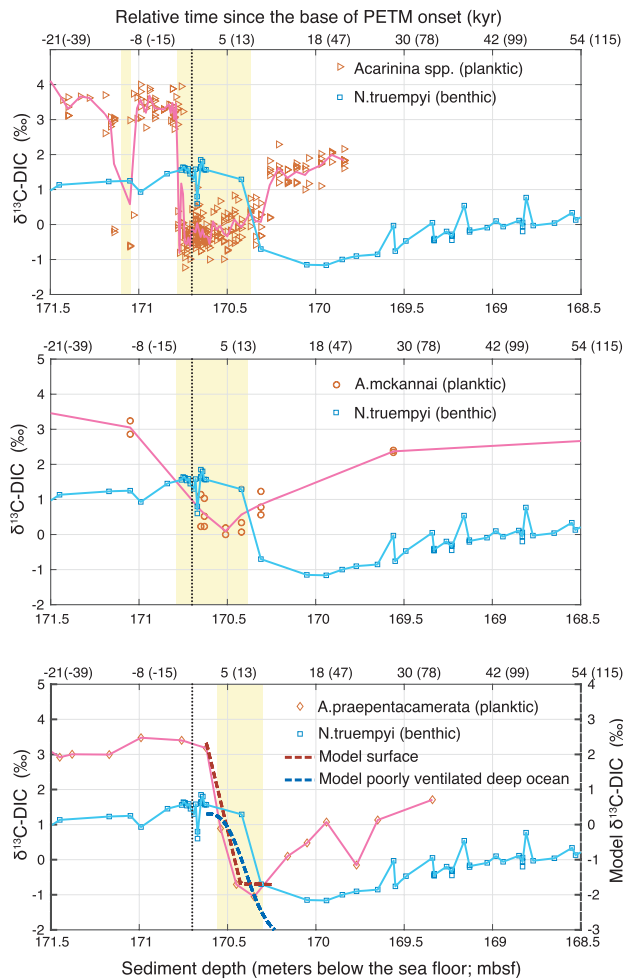
**Projections for the 21st century and sensitivity experiments.** As a primary source of uncertainty in future projection, we consider the geochemical effects of different CO<sub>2</sub> emission scenarios, as represented by the four RCPs (i.e., RCP2.6,



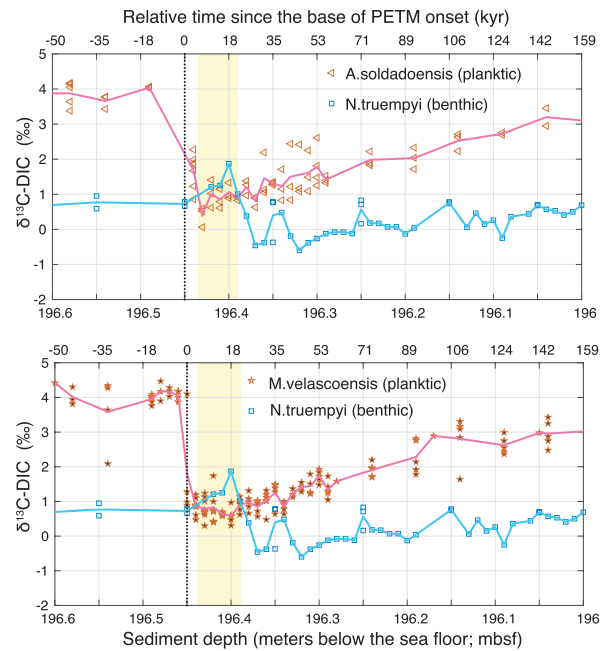
**a** Industrial time oceanic  $\delta^{13}\text{C-DIC}$  for hypothetical future



**b** Early PETM evolution of oceanic  $\delta^{13}\text{C-DIC}$  at ODP 690



**c** Early PETM evolution of oceanic  $\delta^{13}\text{C-DIC}$  at ODP 1209



RCP4.5, RCP6.0, and RCP8.5)<sup>24</sup>. To this end, we use a model configuration, considered as a typical model setup in carbon isotope modeling<sup>3,28,67</sup>, taken from the Monte Carlo experiment (the “full” model setup in Supplementary Table 1). Using the full model setup, we assume that the ocean circulation, air-sea CO<sub>2</sub> exchange rates including sea ice effects, and sea surface temperature and salinity

remain unchanged with time throughout the simulation. An uncertainty associated with this assumption is tested in Supplementary Note 3 where we relax the assumption of unchanged air-sea CO<sub>2</sub> exchange rates, and sea surface temperature and salinity using the Community Earth System Model version 2 (CESM2)-based estimates<sup>39,68</sup>. We also assume that the same linear relationship between

**Fig. 6  $\delta^{13}\text{C}$ -DIC changes during industrial times and early PETM.** **a** Estimates of surface and deep ocean (2–3 km)  $\delta^{13}\text{C}$ -DIC averaged over the global ocean are shown. The Monte Carlo experiment-based estimates from 1800 to 2018 are combined with our projections from 2019 to 5000, assuming that atmospheric  $\delta^{13}\text{C}$ - $\text{CO}_2$  remains constant after the year 2500. The time periods over which the globally averaged surface  $\delta^{13}\text{C}$ -DIC values fall below the globally averaged deep ocean  $\delta^{13}\text{C}$ -DIC values are highlighted as yellow shading. The duration of the vertical gradient reversal is sensitive to the geographic locations, as shown for the North Atlantic (N.Atl., north of 20°N) and the North Pacific (N.Pac., north of 20°N). **b** Red and blue scatters show planktic and benthic foraminifera  $\delta^{13}\text{C}$  records, respectively, from ODP Site 690 (South Atlantic, 65°S, 1°E, 2100 m deep). Red and blue solid lines show linear interpolations of the respective scatters, after averaging the data with a 0.01 mbsf bin interval of sediment depth. The top X-axis labels denote the relative ages since the base of the PETM onset. The relative age outside parentheses is based on Thomas and Shackleton<sup>42</sup> while the relative age based on Bains et al.<sup>43</sup> is shown inside parentheses. The base of the PETM onset is denoted as a vertical dotted line and taken from Nunes and Norris<sup>10</sup>. The periods over which planktic  $\delta^{13}\text{C}$  values are lower than benthic  $\delta^{13}\text{C}$  values are highlighted as yellow shading. In the bottom panel of **(b)**, we overlay the red and blue dashed lines, showing the model-based estimates of the globally averaged surface  $\delta^{13}\text{C}$ -DIC and an averaged  $\delta^{13}\text{C}$ -DIC at 2–3 km depths of the North Pacific, taken from Fig. 5b red solid and green dashed lines, respectively. The positions of both dashed lines are shifted such that the positions for initial declining match between the foraminifera records and the simulation. **c** Same as **b** except that the data from ODP Site 1209 (North Pacific, 33°N, 159°E, 2387 m deep) is shown. The base of the PETM onset (vertical dotted line) is taken from Petrizzo<sup>76</sup>. The age model is from Westerhold et al.<sup>41</sup>.

atmospheric  $\text{CO}_2$  and the  $\delta^{13}\text{C}$ - $\text{CO}_2$ , derived based on the observations over 1980–2018 (Supplementary Fig. 3), holds for the atmosphere from 2019 to 2100.

We also perform two idealized experiments in order to elucidate how changing oceanic carbon chemistry affects the oceanic  $\delta^{13}\text{C}$ -DIC changes. In order to suppress the effect of changing oceanic carbonate chemistry, we perform “fixed. $\text{CO}_2$ ” experiment that is identical to the full model setup except that the atmospheric  $\text{CO}_2$  is fixed at a preindustrial value of 280 ppm while the  $\delta^{13}\text{C}$  of atmospheric  $\text{CO}_2$  is changing as in the full model setup. Thus, the difference between the full model setup and the “fixed. $\text{CO}_2$ ” setup indicates the effects of increasing oceanic DIC on simulated oceanic  $\delta^{13}\text{C}$ -DIC changes, which are dominated by the effects of enhanced air-sea carbon isotope equilibration rates under higher DIC conditions<sup>40</sup>. In order to explore the effect of changing oceanic carbonate chemistry on the natural component of oceanic  $\delta^{13}\text{C}$ -DIC, we also perform “fixed.ratio” experiment where atmospheric  $\text{CO}_2$  changes as in the full model setup while the  $\delta^{13}\text{C}$ - $\text{CO}_2$  remains fixed at a preindustrial value of  $-6.5\%$ . The difference between the full model setup and “fixed.ratio” setup is then interpreted as an effect of changing carbonate chemistry on natural  $\delta^{13}\text{C}$ -DIC. In the “fixed.ratio” model, we turn off the kinetic fractionations during air-sea  $\text{CO}_2$  exchange and the  $\text{CO}_2$ -dependent photosynthetic fractionations in order to focus only on the effect of changing DIC on the redistribution of  $\delta^{13}\text{C}$ -DIC. Because the combined effects of kinetic fractionations and the  $\text{CO}_2$ -dependent photosynthetic fractionations are negligible with values within  $\pm 0.1\%$  for all RCP scenarios, whether we turn on or off both effects in the “fixed.ratio” setup do not make discernible differences in our interpretations of the experiment results.

**Multi-millennial simulations for hypothetical futures.** Although not a primary focus in this study, we also perform multi-millennial simulations to explore how sensitive the magnitude and duration of the vertical  $\delta^{13}\text{C}$ -DIC gradient reversal are to the RCP scenarios. In these hypothetical deep future simulations, we extend the RCP-based future projections by assuming that atmospheric  $\text{CO}_2$  and its  $\delta^{13}\text{C}$ - $\text{CO}_2$  stay constant from the year 2500 to a year 8000 at the values of the year of 2500. Specifically, the RCP scenarios for atmospheric  $\text{CO}_2$  until the year of 2500 are taken from Moss et al.<sup>24</sup> and the same linear relationship between atmospheric  $\text{CO}_2$  and  $\delta^{13}\text{C}$ - $\text{CO}_2$  used for our 21st century projections are assumed for the extended future simulations. Both atmospheric  $\text{CO}_2$  and its isotopic signature are kept constant from the year of 2500 onwards until the vertical  $\delta^{13}\text{C}$ -DIC gradients are recovered. We use the full model setup without considering changes in ocean circulation, air-sea gas exchange rates, and biogeochemical processes.

**Sensitivity experiments with estimated PETM atmospheric  $\text{CO}_2$ .** Based on the present-day ocean model configurations (See below), we use two estimates of the early PETM atmospheric  $\text{CO}_2$  changes following Penman and Zachos<sup>19</sup> and Cui et al.<sup>8</sup>. The two estimates are chosen because they represent both sides of the spectrum for the PETM onset period of 3–20 kyr<sup>8,12,20,69</sup>. In the “rapid” setup, atmospheric  $\text{CO}_2$  linearly increases from 750 to 1500 ppm over 5 kyr according to Penman and Zachos<sup>19</sup>. The “rapid” setup is branched into two experiments with two different maximum atmospheric  $\delta^{13}\text{C}$ - $\text{CO}_2$  excursions of  $-4\%$  (refs. 8,70) and  $-5\%$ , the latter corresponding to a typical  $\delta^{13}\text{C}$  excursion of land plants during the PETM<sup>70</sup>. Atmospheric  $\delta^{13}\text{C}$ - $\text{CO}_2$  is assumed to linearly decrease from  $-6.5\%$  at a model year of zero to either  $-10.5\%$  and  $-11.5\%$  at a model year of 5 kyr, which corresponds to the atmospheric  $\text{CO}_2$  perturbation period. In the “slow” setup, atmospheric  $\text{CO}_2$  linearly increases from 834 ppm to either 1500 ppm or 4200 ppm over 20 kyr, as denoted as “ $\times 2$ ” and “ $\times 5$ ” scenarios respectively, following Cui et al.<sup>8</sup>. Both “ $\times 2$ ” and “ $\times 5$ ” experiments use the same atmospheric  $\delta^{13}\text{C}$ - $\text{CO}_2$  excursion of  $-4\%$ , by assuming that atmospheric  $\delta^{13}\text{C}$ - $\text{CO}_2$  decreases from  $-6.5\%$  at a model year of zero to  $-10.5\%$  at a model year of 20 kyr, which corresponds to the atmospheric  $\text{CO}_2$  perturbation period.

In both “rapid” and “slow” setups, we use two ocean circulation states: the present-day ocean circulation as in the full model setup and a circulation where an

averaged deep ocean (2–3 km depth) ventilation age is three times larger at 2237 years compared to 758 years for the present-day ocean (See Supplementary Fig. 10 for the distribution of deep ocean ventilation age). The slow ocean ventilation state was previously named as “KL” model in Kwon et al.<sup>71</sup>, and has slower meridional overturning rates of 12 Sv (1 Sv =  $10^6 \text{ m}^3 \text{ s}^{-1}$ ) for the North Atlantic Deep Water and 5 Sv for the Antarctic Bottom Water, compared to the present-day circulation model<sup>49</sup> of 20 Sv and 16 Sv, respectively. Despite the different overturning rates and ventilation states, both circulation models are based on the present-day configurations of ocean bathymetry and atmospheric buoyancy and momentum forcing. Therefore, none of the circulation states might represent a plausible state for the PETM. Nevertheless, the PETM ocean would still have regions of relatively well-ventilated and poorly ventilated deep waters<sup>44,45</sup>, although they would not correspond to the North Atlantic and North Pacific, respectively, for the present-day configuration. Hence, the basin-scale contrast in deep ocean  $\delta^{13}\text{C}$ -DIC responses should be regarded as a contrast between well vs. poorly ventilated deep waters.

We only explore the geochemical effects from changing atmospheric  $\text{CO}_2$  and  $\delta^{13}\text{C}$ - $\text{CO}_2$  on  $\delta^{13}\text{C}$ -DIC changes, assuming that ocean circulation, ocean temperature, air-sea  $\text{CO}_2$  exchange rates, and marine biological pump remain fixed at those from the present-day ocean throughout the multimillennial simulations.

**Foraminifera  $\delta^{13}\text{C}$  records for the PETM onset.** We revisit the early PETM evolutions of surface and deep ocean  $\delta^{13}\text{C}$ -DIC, as inferred from planktic and benthic foraminifera  $\delta^{13}\text{C}$  records, using the latest compilation of Shaw et al.<sup>25</sup>. Two ODP Sites 690 and 1209 are chosen for the PETM records because the two ODP sites are located in the open ocean and their  $\delta^{13}\text{C}$  records have high temporal resolutions, the latter which is crucial for resolving the  $\delta^{13}\text{C}$ -DIC evolution during the PETM onset. We assume that the  $\delta^{13}\text{C}$  values of mixed layer planktic foraminifera represent the surface  $\delta^{13}\text{C}$ -DIC whereas the  $\delta^{13}\text{C}$  values of epifaunal benthic foraminifera represent the  $\delta^{13}\text{C}$ -DIC at the depths of the ODP sites. Those inferred  $\delta^{13}\text{C}$ -DIC values are then compared with our model-based estimates averaged over 0–74 m depths for planktic and over 2–3 km depths for benthic.

The original sources of data presented in Fig. 6b, c are as follows: For the ODP Site 690 (South Atlantic, 65°S, 1°E, 2100 m deep), the  $\delta^{13}\text{C}$  records of *N.truempyi*, *Acarinina* spp., *A.mckannai*, *A.praepentacamerata* are from refs. 13,42,72–74. For the ODP Site 1209 (North Pacific, 33°N, 159°E, 2387 m deep), the  $\delta^{13}\text{C}$  records of *N.truempyi* are from ref. 41, the *A.soldadoensis* data are from ref. 75, and the *M.velascoensis* data are from refs. 69,75. No corrections are applied to the foraminifera  $\delta^{13}\text{C}$  records because of the lack of information. Nevertheless, uncertainties are likely small in this single species comparison at the two open ocean sites where a reduced photosymbiosis has been reported for the PETM *acarininids* and *morozovellids* (therefore less offset from seawater  $\delta^{13}\text{C}$ -DIC)<sup>25</sup>. The age models for the foraminifera  $\delta^{13}\text{C}$  records are from Thomas and Shackleton<sup>42</sup> and Bains et al.<sup>43</sup> for ODP Site 690 and Westerhold et al.<sup>41</sup> for ODP Site 1209.

## Data availability

The global database for the present-day  $\delta^{13}\text{C}$  of DIC is available at <https://www.ncdc.noaa.gov/paleo-search/study/21750>. The latest compilations of foraminifera  $\delta^{13}\text{C}$  for the PETM are available at <https://doi.pangaea.de/10.1594/PANGAEA.922272> and <https://doi.pangaea.de/10.1594/PANGAEA.922292>. The atmospheric  $\text{CO}_2$  and its isotopic composition data used for model forcing are from [https://scrippsco2.ucsd.edu/data/atmospheric\\_co2/](https://scrippsco2.ucsd.edu/data/atmospheric_co2/). The sea surface temperature data used in this study are from <https://www.metoffice.gov.uk/hadobs/hadisst/data/download.html>, <https://www.esrl.noaa.gov/psd/data/gridded/data.noaa.erst.v5.html>, and <https://www.esrl.noaa.gov/psd/data/gridded/data.cobe2.html>. The projected atmospheric  $\text{CO}_2$  concentrations for the four RCP scenarios are available at <https://tntcat.iiasa.ac.at/RcpDb/>. The CESM2 Large Ensemble Simulations are available at <https://www.cesm.ucar.edu/projects/community-projects/LENS2/datasets.html>.

All of the model results presented here are made available at <https://climatedata.ibs.re.kr/data/papers/kwon-et-al-2022-commsenv>.

**Code availability**

The model code, written in MATLAB, will be made available from the corresponding author on reasonable request.

Received: 16 July 2021; Accepted: 16 February 2022;

Published online: 15 March 2022

**References**

- Eide, M., Olsen, A., Ninnemann, U. S. & Eldevik, T. A global estimate of the full oceanic  $^{13}\text{C}$  Suess effect since the preindustrial. *Global Biogeochem. Cycles* **31**, 492–514 (2017).
- Keeling, C. D. The Suess effect:  $^{13}\text{C}$  carbon- $^{14}\text{C}$  carbon interrelations. *Environ. Int.* **2**, 229–300 (1979).
- Schmittner, A. et al. Biology and air-sea gas exchange controls on the distribution of carbon isotope ratios ( $\delta^{13}\text{C}$ ) in the ocean. *Biogeosciences* **10**, 5793–5816 (2013).
- Schmittner, A. et al. Calibration of the carbon isotope composition ( $\delta^{13}\text{C}$ ) of benthic foraminifera. *Paleoceanography* **32**, 512–530 (2017).
- Goericke, R. & Fry, B. Variations of marine plankton  $\delta^{13}\text{C}$  with latitude, temperature, and dissolved  $\text{CO}_2$  in the world ocean. *Global Biogeochem. Cycles* **8**, 85–90 (1994).
- Lynch-Stieglitz, J., Stocker, T. F., Broecker, W. S. & Fairbanks, R. G. The influence of air-sea exchange on the isotopic composition of oceanic carbon: observations and modeling. *Global Biogeochem. Cycles* **9**, 653–665 (1995).
- Zhang, J., Quay, P. D. & Wilbur, D. O. Carbon-isotope fractionation during gas-water exchange and dissolution of  $\text{CO}_2$ . *Geochim. Cosmochim. Acta* **59**, 107–114 (1995).
- Cui, Y. et al. Slow release of fossil carbon during the Palaeocene–Eocene Thermal Maximum. *Nat. Geosci.* **4**, 481–485 (2011).
- Zachos, J. C. et al. The Palaeocene–Eocene carbon isotope excursion: constraints from individual shell planktonic foraminifer records. *Phil. Trans. R. Soc. A* **365**, 1829–1842 (2007).
- Nunes, F. & Norris, R. D. Abrupt reversal in ocean overturning during the Palaeocene/Eocene warm period. *Nature* **439**, 60–63 (2006).
- Kirtland Turner, S. & Ridgwell, A. Development of a novel empirical framework for interpreting geological carbon isotope excursions, with implications for the rate of carbon injection across the PETM. *Earth Planet. Sci. Lett.* **435**, 1–13 (2016).
- McInerney, F. A. & Wing, S. L. The Paleocene-Eocene thermal maximum: a perturbation of carbon cycle, climate, and biosphere with implications for the future. *Annu. Rev. Earth Planet. Sci.* **39**, 489–516 (2011).
- Kennett, J. P. & Stott, L. D. Abrupt deep-sea warming, paleoceanographic changes and benthic extinctions at the end of the Palaeocene. *Nature* **353**, 225–229 (1991).
- Tipple, B. J., Meyers, S. R. & Pagani, M. Carbon isotope ratio of Cenozoic  $\text{CO}_2$ : a comparative evaluation of available geochemical proxies. *Paleoceanography* (2010).
- Hodell, D. A., Venz, K. A., Charles, C. D. & Ninnemann, U. S. Pleistocene vertical carbon isotope and carbonate gradients in the South Atlantic sector of the Southern Ocean. *Geochem. Geophys. Geosyst.* **4**, 1–19 (2003).
- Gebbie, G., Peterson, C. D., Lisiecki, L. E. & Spero, H. J. Global-mean marine  $\delta^{13}\text{C}$  and its uncertainty in a glacial state estimate. *Quat. Sci. Rev.* **125**, 144–159 (2015).
- Norris, R. D., Kirtland Turner, S., Hull, P. M. & Ridgwell, A. Marine ecosystem responses to Cenozoic global change. *Science* **341**, 492–498 (2013).
- Haynes, L. L. & Honisch, B. The seawater carbon inventory at the Paleocene-Eocene Thermal Maximum. *Proc. Natl Acad. Sci. USA* **117**, 24088–24095 (2020).
- Penman, D. E. & Zachos, J. C. New constraints on massive carbon release and recovery processes during the Paleocene–Eocene Thermal Maximum. *Environ. Res. Lett.* (2018).
- Zeebe, R. E., Ridgwell, A. & Zachos, J. C. Anthropogenic carbon release rate unprecedented during the past 66 million years. *Nat. Geosci.* **9**, 325–329 (2016).
- Kirtland Turner, S., Hull, P. M., Kump, L. R. & Ridgwell, A. A probabilistic assessment of the rapidity of PETM onset. *Nat. Commun.* **8**, 353 (2017).
- DeVries, T. The oceanic anthropogenic  $\text{CO}_2$  sink: storage, air-sea fluxes, and transports over the industrial era. *Global Biogeochem. Cycles* **28**, 631–647 (2014).
- Kwon, E. Y. et al. Stable carbon isotopes suggest large terrestrial carbon inputs to the global ocean. *Global Biogeochem. Cycles* **35**, e2020GB006684 (2021).
- Moss, R. H. et al. The next generation of scenarios for climate change research and assessment. *Nature* **463**, 747–756 (2010).
- Shaw, J. O. et al. Photosymbiosis in planktonic foraminifera across the Paleocene–Eocene thermal maximum. *Paleobiology* **47**, 632–647 (2021).
- Holden, P. B. et al. Controls on the spatial distribution of oceanic  $\delta^{13}\text{C}_{\text{DIC}}$ . *Biogeosciences* **10**, 1815–1833 (2013).
- Sonnerup, R. E. et al. Anthropogenic  $\delta^{13}\text{C}$  changes in the North Pacific Ocean reconstructed using a multiparameter mixing approach (MIX). *Tellus* **59B**, 303–317 (2007).
- Liu, B., Six, K. D. & Ilyina, T. Incorporating the stable carbon isotope  $^{13}\text{C}$  in the ocean biogeochemical component of the Max Planck Institute Earth System Model. *Biogeosciences* **18**, 4389–4429 (2021).
- Swart, P. K. et al. The  $^{13}\text{C}$  Suess effect in scleractinian corals mirror changes in the anthropogenic  $\text{CO}_2$  inventory of the surface oceans. *Geophys. Res. Lett.* **37**, L05604 (2010).
- McNeil, B. I., Matear, R. J. & Tilbrook, B. Does carbon 13 track anthropogenic  $\text{CO}_2$  in the Southern Ocean? *Global Biogeochem. Cycles* **15**, 597–613 (2001).
- Körtzinger, A., Quay, P. D. & Sonnerup, R. E. Relationship between anthropogenic  $\text{CO}_2$  and the  $^{13}\text{C}$  Suess effect in the North Atlantic Ocean. *Global Biogeochem. Cycles* **17**, 1005 (2003).
- Morée, A. L., Schwinger, J. & Heinze, C. Southern Ocean controls of the vertical marine  $\delta^{13}\text{C}$  gradient – a modelling study. *Biogeosciences* **15**, 7205–7223 (2018).
- Eide, M., Olsen, A., Ninnemann, U. S. & Johannessen, T. A global ocean climatology of preindustrial and modern ocean  $\delta^{13}\text{C}$ . *Global Biogeochem. Cycles* **31**, 515–534 (2017).
- Olsen, A. & Ninnemann, U. S. Large  $\delta^{13}\text{C}$  gradients in the preindustrial North Atlantic revealed. *Science* **330**, 658–659 (2010).
- Curry, W. B. & Oppo, D. W. Glacial water mass geometry and the distribution of  $\delta^{13}\text{C}$  of  $\Sigma\text{CO}_2$  in the western Atlantic Ocean. *Paleoceanography* **20**, PA1017 (2005).
- Keeling, C. D. et al. In *A History of Atmospheric  $\text{CO}_2$  and its effects on Plants, Animals, and Ecosystems* (eds Ehleringer, J. R., Cerling, T. E. & Dearing, M. D.) (Springer Verlag, 2005).
- Kwiatkowski, L. et al. Twenty-first century ocean warming, acidification, deoxygenation, and upper-ocean nutrient and primary production decline from CMIP6 model projections. *Biogeosciences* **17**, 3439–3470 (2020).
- Schlunegger, S. et al. Emergence of anthropogenic signals in the ocean carbon cycle. *Nat. Clim. Change* **9**, 719–725 (2019).
- Rodgers, K. B. et al. Ubiquity of human-induced changes in climate variability. *Earth Syst. Dynamics* **12**, 1393–1411 (2021).
- Galbraith, E. D., Kwon, E. Y., Bianchi, D., Hain, M. P. & Sarmiento, J. L. The impact of atmospheric  $\text{pCO}_2$  on carbon isotope ratios of the atmosphere and ocean. *Global Biogeochem. Cycles* **29**, 307–324 (2015).
- Westerhold, T., Röhl, U., Donner, B. & Zachos, J. C. Global extent of early Eocene hyperthermal events: a new Pacific benthic foraminiferal isotope record from Shatsky Rise (ODP Site 1209). *Paleoceanogr. Paleoclimatol.* **33**, 626–642 (2018).
- Thomas, E. & Shackleton, N. The Paleocene-Eocene benthic foraminiferal extinction and stable isotope anomalies. 401–441 (1996).
- Bains, S., Corfield, R. M. & Norris, R. D. Mechanisms of climate warming at the end of the Paleocene. *Science* **285**, 724–727 (1999).
- Ilyina, T. & Heinze, M. Carbonate dissolution enhanced by ocean stagnation and respiration at the onset of the Paleocene-Eocene Thermal Maximum. *Geophys. Res. Lett.* **46**, 842–852 (2019).
- Winguth, A. M. E., Thomas, E. & Winguth, C. Global decline in ocean ventilation, oxygenation, and productivity during the Paleocene-Eocene Thermal Maximum: implications for the benthic extinction. *Geology* **40**, 263–266 (2012).
- Bice, K. L. & Marotzke, J. Could changing ocean circulation have destabilized methane hydrate at the Paleocene/Eocene boundary? *Paleoceanography* **17**, 1018 (2002).
- Abbott, A. N., Haley, B. A., Tripathi, A. K. & Frank, M. Constraints on ocean circulation at the Paleocene–Eocene Thermal Maximum from neodymium isotopes. *Clim. Past* **12**, 837–847 (2016).
- Zachos, J., Pagani, M., Sloan, L., Thomas, E. & Billups, K. Trends, rhythms, and aberrations in global climate 65 Ma to present. *Science* **292**, 686–693 (2001).
- DeVries, T. & Holzer, M. Radiocarbon and helium isotope constraints on deep ocean ventilation and mantle- $^3\text{He}$  sources. *J. Geophys. Res.: Oceans* **124**, 3036–3057 (2019).
- Najjar, R. G. et al. Impact of circulation on export production, dissolved organic matter, and dissolved oxygen in the ocean: results from Phase II of the Ocean Carbon-cycle Model Intercomparison Project (OCMIP-2). *Global Biogeochem. Cycles* (2007).
- Kwon, E. Y. & Primeau, F. Optimization and sensitivity of a global biogeochemistry ocean model using combined in situ DIC, alkalinity, and phosphate data. *J. Geophys. Res.* (2008).
- MacFarling Meure, C. et al. Law Dome  $\text{CO}_2$ ,  $\text{CH}_4$  and  $\text{N}_2\text{O}$  ice core records extended to 2000 years BP. *Geophys. Res. Lett.* (2006).
- Rubino, M. et al. A revised 1000 year atmospheric  $\delta^{13}\text{C}$ - $\text{CO}_2$  record from Law Dome and South Pole, Antarctica. *J. Geophys. Res.* **118**, 8482–8499 (2013).



54. Rayner, N. A. et al. Global analyses of sea surface temperature, sea ice, and night marine air temperature since the late nineteenth century. *J. Geophys. Res. Atmos.* **108**, 4407 (2003).
55. Huang, B. Y. et al. Extended reconstructed sea surface temperature, version 5 (ERSSTv5): upgrades, validations, and intercomparisons. *J. Clim.* **30**, 8179–8205 (2017).
56. Hirahara, S., Ishii, M. & Fukuda, Y. Centennial-scale sea surface temperature analysis and its uncertainty. *J. Clim.* **27**, 57–75 (2014).
57. Peterson, B. J. & Fry, B. Stable isotopes in ecosystem studies. *Ann. Rev. Ecol. Syst.* **18**, 293–320 (1987).
58. Maher, D. T., Santos, I. R., Golsby-Smith, L., Gleeson, J. & Eyre, B. D. Groundwater-derived dissolved inorganic and organic carbon exports from a mangrove tidal creek: The missing mangrove carbon sink? *Limnol. Oceanogr.* **58**, 475–488 (2013).
59. Szymczycha, B., Maciejewska, A., Winogradow, A. & Pempkowiak, J. Could submarine groundwater discharge be a significant carbon source to the southern Baltic Sea? *Oceanologia* **56**, 327–347 (2014).
60. Duarte, C. M. Reviews and syntheses: hidden forests, the role of vegetated coastal habitats in the ocean carbon budget. *Biogeosciences* **14**, 301–310 (2017).
61. Wanninkhof, R. Relationship between wind-speed and gas exchange over the ocean. *J. Geophys. Res.* **97**, 7373–7382 (1992).
62. Sweeney, C. et al. Constraining global air–sea gas exchange for CO<sub>2</sub> with recent bomb <sup>14</sup>C measurements. *Global Biogeochem. Cycles* (2007).
63. Wanninkhof, R. et al. Global ocean carbon uptake: magnitude, variability and trends. *Biogeosciences* **10**, 1983–2000 (2013).
64. Popp, B. N., Takigiku, R., Hayes, J. M., Louda, J. W. & Baker, E. W. The post-Paleozoic chronology and mechanism of <sup>13</sup>C depletion in primary marine organic matter. *Am. J. Sci.* **289**, 436–454 (1989).
65. Freeman, K. H. & Hayes, J. M. Fractionation of carbon isotopes by phytoplankton and estimates of ancient CO<sub>2</sub> levels. *Global Biogeochem. Cycles* **6**, 185–198 (1992).
66. Milliman, J. D. Production and accumulation of calcium carbonate in the ocean: budget of a nonsteady state. *Global Biogeochem. Cycles* **7**, 927–957 (1993).
67. Jahn, A. et al. Carbon isotopes in the ocean model of the Community Earth System Model (CESM1). *Geosci. Model Dev.* **8**, 2419–2434 (2015).
68. Danabasoglu, G. et al. The Community Earth System Model Version 2 (CESM2). *J. Adv. Modeling Earth Syst.* **12**, e2019MS001916 (2020).
69. Penman, D. E., Hönisch, B., Zeebe, R., Thomas, E. & Zachos, J. C. Rapid and sustained surface ocean acidification during the Paleocene-Eocene Thermal Maximum. *Paleoceanography* **29**, 357–369 (2014).
70. Smith, F., Wing, S. L. & Freeman, K. Magnitude of the carbon isotope excursion at the Paleocene-Eocene Thermal Maximum: the role of plant community change. *Earth Planet. Sci. Lett.* **262**, 50–65 (2007).
71. Kwon, E. Y., Sarmiento, J. L., Toggweiler, J. R. & DeVries, T. The control of atmospheric pCO<sub>2</sub> by ocean ventilation change: the effect of the oceanic storage of biogenic carbon. *Global Biogeochem. Cycles* (2011).
72. Kelly, D. C., Zachos, J. C., Bralower, T. J. & Schellenberg, S. A. Enhanced terrestrial weathering/runoff and surface ocean carbonate production during the recovery stages of the Paleocene-Eocene thermal maximum. *Paleoceanography* **20**, PA4024 (2005).
73. Thomas, E., Zachos, J. C. & Bralower, T. J. *Deep-sea environments on a warm earth: latest Paleocene-early Eocene*. 132–160 (Cambridge University Press, 1999).
74. Thomas, D. J., Zachos, J. C., Bralower, T. J., Thomas, E. & Bohaty, S. Warming the fuel for the fire: evidence for the thermal dissociation of methane hydrate during the Paleocene-Eocene thermal maximum. *Geology* **30**, 1067–1070 (2002).
75. Zachos, J. C. et al. A transient rise in tropical sea surface temperature during the Paleocene-Eocene Thermal Maximum. *Science* **302**, 1551–1554 (2003).
76. Petrizzo, M. R. The onset of the Paleocene-Eocene Thermal Maximum (PETM) at Sites 1209 and 1210 (Shatsky Rise, Pacific Ocean) as recorded by planktonic foraminifera. *Mar. Micropaleontol.* **63**, 187–200 (2007).

### Acknowledgements

We acknowledge Jack Shaw and Simon D’haenens who shared their compiled foraminifera  $\delta^{13}\text{C}$  data and provided valuable comments on paleoceanography data. We thank Cedric John for a discussion of foraminifera  $\delta^{13}\text{C}$  measurements. We also thank Eric Galbraith and Tim DeVries for discussions, which helped us motivate this work. We are grateful to Anne Morée and anonymous reviewers for helping us improve the manuscript. E.Y.K. and A.T. are funded by IBS-R028-D1. E.Y.K. also received support through NRF-2016R1D1A1B04931356. A.S. is funded by NSF grant 1924215.

### Author contributions

E.Y.K. and A.T. conceived the idea of the future projection of oceanic  $\delta^{13}\text{C}$ -DIC and a comparison with the PETM  $\delta^{13}\text{C}$  excursions. B.T. and A.S. helped further shape the idea. E.Y.K. carried out the numerical experiments and analyses of  $\delta^{13}\text{C}$  data, and wrote the manuscript with inputs from all the coauthors.

### Competing interests

The authors declare no competing interests.

### Additional information

**Supplementary information** The online version contains supplementary material available at <https://doi.org/10.1038/s43247-022-00388-8>.

**Correspondence** and requests for materials should be addressed to Eun Young Kwon.

**Peer review information** *Communications Earth & Environment* thanks Anne Morée and the other, anonymous, reviewer(s) for their contribution to the peer review of this work. Primary Handling Editors: Sze Ling Ho and Clare Davis. Peer reviewer reports are available.

**Reprints and permission information** is available at <http://www.nature.com/reprints>

**Publisher’s note** Springer Nature remains neutral with regard to jurisdictional claims in published maps and institutional affiliations.



**Open Access** This article is licensed under a Creative Commons Attribution 4.0 International License, which permits use, sharing, adaptation, distribution and reproduction in any medium or format, as long as you give appropriate credit to the original author(s) and the source, provide a link to the Creative Commons license, and indicate if changes were made. The images or other third party material in this article are included in the article’s Creative Commons license, unless indicated otherwise in a credit line to the material. If material is not included in the article’s Creative Commons license and your intended use is not permitted by statutory regulation or exceeds the permitted use, you will need to obtain permission directly from the copyright holder. To view a copy of this license, visit <http://creativecommons.org/licenses/by/4.0/>.

© The Author(s) 2022